# Frequency- and Bandwidth-Tunable Bandstop Filter Containing Variable Coupling Between Transmission Line and Resonator

Seong-Wook Jeong and Juseop Lee, *Senior Member, IEEE*

***Abstract*— This paper presents a frequency- and bandwidth-tunable bandstop filter using substrate-integrated waveguide (SIW) resonators. For designing such a filter, this paper also presents a tunable coupling structure between a microstrip line and an SIW resonator for obtaining the bandwidth tuning capability. The coupling structure has two coupling slots between the microstrip line and the resonator, and the phase shift between the two slots determines the overall external coupling value of the resonator. This external coupling value can be controlled by making use of a phase shifter, which in turn makes it possible to adjust the bandwidth of a bandstop filter. A thorough mathematical analysis is shown using the equivalent circuit model of the presented coupling structure, and it has been verified by measuring an SIW resonator containing the presented structure. The presented tunable coupling structure has also been applied to a design of bandstop filter that can be tuned from 2.8 to 3.4 GHz. The measured results at 3.1 GHz show that the bandwidth can be tuned from 0 (all-pass) to 96 MHz reaching the attenuation level of 44 dB.**

***Index Terms*— All-pass filter, bandstop filter, bandwidth tunable, frequency tunable, substrate-integrated waveguide (SIW) resonator.**

## I. Introduction

RECENTLY, tunable microwave filters have been of a great interest as wireless systems are designed to be flexible ones capable of occupying various bandwidths. Many technologies have been explored but most studies have been focused on designing tunable bandpass filters [1]–[8]. Although tunable bandstop filters have not been investigated extensively in comparison with tunable bandpass filters, a number of useful design techniques for bandstop filters using distributed resonators have been presented [9]–[18]. Planar tunable bandstop filters are presented in [9]–[15] and tunable bandstop filters in waveguide structure are discussed in [16]–[18]. In general, a bandstop filter containing distributed resonators has a transmission line running from the source (input port) to the load (output port) and resonators are coupled to the line being separated by odd multiples of a quarter wavelength along the line.

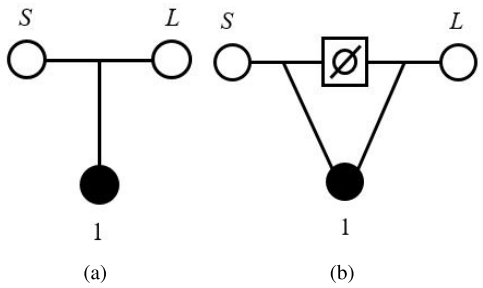


Fig. 1. Coupling routing diagram. (a) Conventional bandstop filter. (b) Proposed bandstop filter with phase shifter.

The aforementioned tunable bandstop filters are capable of adjusting their center frequencies by virtue of frequency-tunable resonators. However, they have no or limited bandwidth tuning capabilities. The incapability to adjust the bandwidth is due to fact that the coupling between the line and each resonator is static. A number of filters adopt a variable capacitor between the line and each resonator to be able to control the coupling between the line and each resonator, but the zero coupling for achieving the all-pass response cannot be obtained since having the zero capacitance is not feasible. In this paper, a new design methodology for frequency- and bandwidth-tunable bandstop filters is presented. More specifically, a tunable external coupling structure is newly presented for acquiring bandwidth tuning capability including zero bandwidth giving the all-pass response. A detailed mathematical analysis using the equivalent circuit model is provided in this paper. A single substrate-integrated waveguide (SIW) resonator structure containing the presented coupling structure has been fabricated and measured for verifying the theory and analysis. In addition, the presented coupling structure has been applied to a second-order frequency- and bandwidth-tunable bandstop filter design.

## II. Theory

Fig. 1(a) shows the coupling diagram of a conventional first-order bandstop filter. *S* and *L* represent the source and load, respectively, and the number depicts the resonator. In the diagram, the source and load are directly connected to each other and the resonator is connected in the shunt direction. A bandstop filter that corresponds to this diagram usually

Manuscript received November 16, 2016; revised April 19, 2017 and July 6, 2017; accepted August 27, 2017. This work was supported by the Basic Science Research Program through the National Research Foundation of Korea funded by the Ministry of Science, ICT & Future Planning under Grant NRF-2015R1C1A1A02036754. *(Corresponding author: Juseop Lee.)*

The authors are with the Department of Computer and Communications Engineering, Korea University, Seoul 02841, South Korea (e-mail: juseoplee@gmail.com).

Color versions of one or more of the figures in this paper are available online at http://ieeexplore.ieee.org.

Digital Object Identifier 10.1109/TMTT.2017.2756963

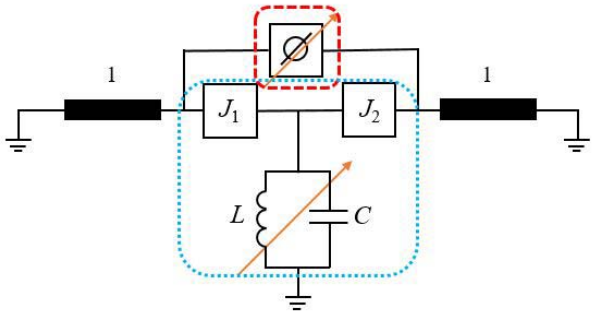


Fig. 2. Circuit model corresponding to the coupling diagram shown in Fig. 1(b). The port admittance is normalized to 1 Ω.

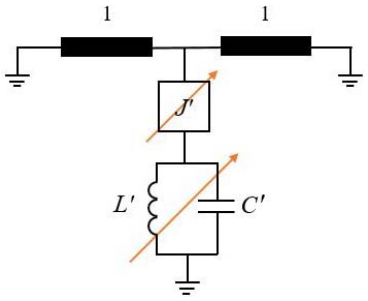


Fig. 3. Circuit model equivalent to the one shown in Fig. 2.

has a uniform transmission line between the source and load and a distributed resonator is coupled to the transmission line. For this classical bandstop filter, the center frequency of the filter is determined by the resonant frequency of the resonator in use, and the bandwidth by the coupling between the resonator and the line. Hence, a frequency-agile feature can be obtained by using a frequency-tunable resonator. However, acquiring a tunable bandwidth usually requires alteration of the physical configuration or electromagnetic wave interaction between the resonator and the line to have a different coupling value between them. This implies that electrically adjusting the coupling value between the resonator and the line is a challenging task, especially when the resonator is of nonplanar structure, and only a few works on this topic for nonplanar resonators have been reported so far [15], [16].

For electrically controlling the coupling value between a resonator and a line, we present an alternative approach. Fig. 1(b) shows the coupling diagram of a first-order bandstop filter used in this paper. The resonator is coupled to the line two times at two different reference points and there is a phase delay from one reference point to the other. Fig. 2 shows the circuit model that corresponds to the coupling diagram shown in Fig. 1(b). $J$'s represent admittance inverters that correspond to external coupling structures between the line and the resonator. There exists a phase shifter between the input and output ports in order to account for the phase delay from one port to the other. In this circuit model, the resonator and phase shifter are tunable while the inverters are static, since the external coupling structure is usually not electrically tunable as mentioned above. In this analysis, the phase shifter is assumed to be independent of the frequency for simplicity, and we will show that the circuit model in Fig. 2 can be considered as a resonator having a tunable coupling structure as shown in Fig. 3. The circuit model in Fig. 2 has two blocks connected in parallel. One consists of the phase shifter and the other is composed of the two inverters and the resonator. Hence, we first find the admittance matrix of each block. The $S$ matrix of the frequency-independent phase shifter is given by

$$\mathbf{S_1} = \begin{bmatrix} 0 & e^{-j\theta} \\ e^{-j\theta} & 0 \end{bmatrix} \tag{1}$$

where $\theta$ is the phase shift value of the phase shifter. It can be converted to the admittance matrix

$$\mathbf{Y_1} = \begin{bmatrix} -\dfrac{j}{\tan\theta} & \dfrac{j}{\sin\theta} \\ \dfrac{j}{\sin\theta} & -\dfrac{j}{\tan\theta} \end{bmatrix}. \tag{2}$$

The admittance matrix of the other block can be found from the $ABCD$ matrix. Since $ABCD$ matrices of the inverter and the resonator are given by

$$\begin{bmatrix} A & B \\ C & D \end{bmatrix} = \begin{bmatrix} 0 & j\dfrac{1}{J} \\ jJ & 0 \end{bmatrix} \tag{3}$$

and

$$\begin{bmatrix} A & B \\ C & D \end{bmatrix} = \begin{bmatrix} 1 & 0 \\ j\left(\omega C - \dfrac{1}{\omega L}\right) & 1 \end{bmatrix} \tag{4}$$

respectively, the $ABCD$ matrix of the block containing the two inverters and the resonator is given by

$$\begin{aligned} &\begin{bmatrix} A & B \\ C & D \end{bmatrix} \\ &= \begin{bmatrix} 0 & j\dfrac{1}{J_1} \\ jJ_1 & 0 \end{bmatrix} \begin{bmatrix} 1 & 0 \\ j\left(\omega C - \dfrac{1}{\omega L}\right) & 1 \end{bmatrix} \begin{bmatrix} 0 & j\dfrac{1}{J_2} \\ jJ_2 & 0 \end{bmatrix} \\ &= \begin{bmatrix} -\dfrac{J_2}{J_1} & -\dfrac{j\left(\omega C - \frac{1}{\omega L}\right)}{J_1 J_2} \\ 0 & -\dfrac{J_1}{J_2} \end{bmatrix}. \end{aligned} \tag{5}$$

Hence, the admittance matrix is found to be

$$\mathbf{Y_2} = \begin{bmatrix} \dfrac{J_1^2}{j\left(\omega C - \frac{1}{\omega L}\right)} & \dfrac{J_1 J_2}{j\left(\omega C - \frac{1}{\omega L}\right)} \\ \dfrac{J_1 J_2}{j\left(\omega C - \frac{1}{\omega L}\right)} & \dfrac{J_2^2}{j\left(\omega C - \frac{1}{\omega L}\right)} \end{bmatrix}. \tag{6}$$

The admittance matrix of the circuit shown in Fig. 2 can be found by adding the two matrices in (2) and (6), and it is given by

$$\begin{aligned} \mathbf{Y} &= \begin{bmatrix} -\dfrac{j}{\tan\theta} & \dfrac{j}{\sin\theta} \\ \dfrac{j}{\sin\theta} & -\dfrac{j}{\tan\theta} \end{bmatrix} + \begin{bmatrix} \dfrac{J_1^2}{jR(\omega)} & \dfrac{J_1 J_2}{jR(\omega)} \\ \dfrac{J_1 J_2}{jR(\omega)} & \dfrac{J_2^2}{jR(\omega)} \end{bmatrix} \\ &= \begin{bmatrix} -\dfrac{j}{\tan\theta} + \dfrac{J_1^2}{jR(\omega)} & \dfrac{j}{\sin\theta} + \dfrac{J_1 J_2}{jR(\omega)} \\ \dfrac{j}{\sin\theta} + \dfrac{J_1 J_2}{jR(\omega)} & -\dfrac{j}{\tan\theta} + \dfrac{J_2^2}{jR(\omega)} \end{bmatrix} \end{aligned} \tag{7}$$

where

$$R(\omega) = \omega C - \frac{1}{\omega L}. \tag{8}$$

For visualizing the frequency response of the circuit model in Fig. 2, $S_{11}$ and $S_{21}$ have been found and they are given in (9) and (10), as shown at the bottom of this page, where

$$\begin{aligned}\Delta Y &= (Y_{11}+Y_0)(Y_{22}+Y_0) - Y_{12}Y_{21} \\ &= \left(1 - \frac{j}{\tan\theta} + \frac{J_1^2}{jR(\omega)}\right)\left(1 - \frac{j}{\tan\theta} + \frac{J_2^2}{jR(\omega)}\right) \\ &\quad - \left(\frac{j}{\sin\theta} + \frac{J_1 J_2}{jR(\omega)}\right)^2. \end{aligned} \tag{11}$$

In (9) and (10), $Y_{\mathrm{mn}}$ is the element in the $m$th row and $n$th column of the admittance matrix in (7), and $Y_0$ is normalized to one.

The black solid lines in Fig. 4 show the frequency responses of the circuit model shown in Fig. 2 when the lumped element values of the resonator have been arbitrarily set to $C = 1591.5$ pF and $L = 1.6561$ pH so that it resonates at 3.1 GHz and the inverter values have been arbitrary chosen to be $J_1 = -J_2 = 1$ for demonstration. The case when $J_1$ and $J_2$ have the same sign will be discussed later.

It is shown in Fig. 4 that the width of the notch varies with the phase shift, and this indicates that the overall effective external coupling value changes. Since this type of the response can be obtained from a circuit containing a tunable resonator and a tunable external coupling structure, it can be concluded that the circuit model shown in Fig. 2 is equivalent to the one in Fig. 3. It is worth noting that the center frequency of the notch moves with the phase shift although the $LC$ resonator is set to resonate at 3.1 GHz. This deviation of the center frequency is of no importance since the center frequency can be adjusted to the desired one by means of using a tunable resonator.

For validating the equivalency between the two circuits, the transmission power ratios of the two circuits are compared. Equation (10) can be written in an alternative form as (12), shown at the bottom of this page, under the condition that $J_1 = -J_2$. At the resonant frequency ($\omega_0$) of the resonator, $R(\omega) = 0$. From (12), the magnitude of $S_{21}$ and $|S_{21}|$ can also be derived, and the notch frequency, $\omega_1$, at which $|S_{21}| = 0$ can be found as

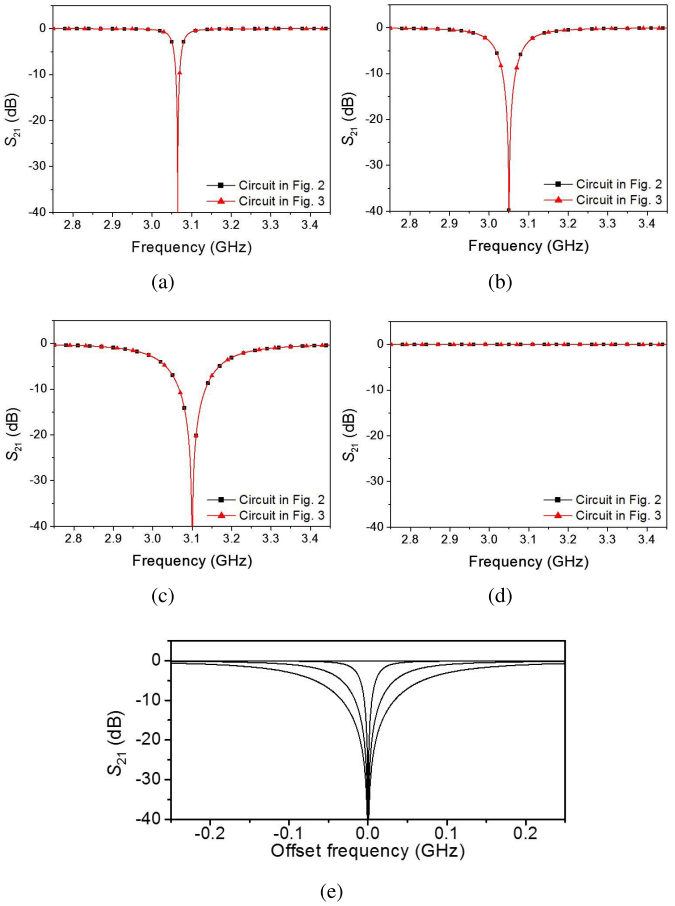


Fig. 4. Black lines with squares show the frequency responses of the circuit model shown in Fig. 2 when $J_1$ and $J_2$ have opposite values when (a) $\theta = \pi/4$, (b) $\theta = \pi/2$, (c) $\theta = \pi$, and (d) $\theta = 2\pi$. In (e), the four curves are shown for observing the bandwidth changing. Red lines with triangles show the frequency responses of the circuit shown in Fig. 3 with the parameters given in Table I.

$$\omega_1 = \frac{\sqrt{J_1^4 \sin^2\theta + 4\omega_0^2 C^2} - J_1^2 \sin\theta}{2C}. \tag{13}$$

It is worth noting that $\omega_1 = \omega_0$ when $\theta = n\pi$ ($n$ = integer) and the notch frequency deviates from $\omega_0$ when $\theta \neq n\pi$, which can be observed in Fig. 4. The transmission coefficient

$$S_{11} = \frac{(Y_0 - Y_{11})(Y_0 + Y_{22}) + Y_{12}Y_{21}}{\Delta Y} = \frac{\left(1 + \frac{j}{\tan\theta} - \frac{J_1^2}{jR(\omega)}\right)\left(1 - \frac{j}{\tan\theta} + \frac{J_2^2}{jR(\omega)}\right) + \left(\frac{j}{\sin\theta} + \frac{J_1 J_2}{jR(\omega)}\right)^2}{\left(1 - \frac{j}{\tan\theta} + \frac{J_1^2}{jR(\omega)}\right)\left(1 - \frac{j}{\tan\theta} + \frac{J_2^2}{jR(\omega)}\right) - \left(\frac{j}{\sin\theta} + \frac{J_1 J_2}{jR(\omega)}\right)^2} \tag{9}$$

$$S_{21} = \frac{-2Y_{21}Y_0}{\Delta Y} = \frac{-2\left(\frac{j}{\sin\theta} + \frac{J_1 J_2}{jR(\omega)}\right)}{\left(1 - \frac{j}{\tan\theta} + \frac{J_1^2}{jR(\omega)}\right)\left(1 - \frac{j}{\tan\theta} + \frac{J_2^2}{jR(\omega)}\right) - \left(\frac{j}{\sin\theta} + \frac{J_1 J_2}{jR(\omega)}\right)^2} \tag{10}$$

$$S_{21} = \frac{R(\omega) + J_1^2 \sin\theta}{R(\omega)\cos\theta + J_1^2 \sin\theta + j\left(R(\omega)\sin\theta + J_1^2(1 - \cos\theta)\right)} \tag{12}$$

TABLE I
PARAMETERS OF THE CIRCUIT IN FIG. 3 FOR REPLICATING THE CIRCUIT IN FIG. 2

| | | Circuit in Fig. 2 | | | |
|---|---|---|---|---|---|
| | | $\theta = \pi/4$ | $\pi/2$ | $\pi$ | $2\pi$ |
| Circuit in Fig. 3 | $J'$ | 0.7659 | 1.4053 | 2.0000 | 0.0000 |
| | $C'$ (pF) | 1591.5 | 1591.5 | 1591.5 | Arbitrary |
| | $L'$ (pH) | 1.6944 | 1.7104 | 1.6561 | Arbitrary |

of the circuit in Fig. 3 can be derived and it is given by

$$S'_{21} = \frac{2}{2 + \frac{J'^2}{jR'(\omega)}} \tag{14}$$

where

$$R'(\omega) = \omega C' - \frac{1}{\omega L'}. \tag{15}$$

At the resonant frequency ($\omega = \omega'_0$), $R'(\omega) = 0$ and $|S'_{21}| = 0$. In other words, the resonant frequency is identical to the notch frequency. One of the $C'$ and $L'$ can be arbitrarily chosen and the other is determined by

$$C'L' = \frac{1}{\omega_1^2} \tag{16}$$

since the notch frequency of the circuit in Fig. 2 is $\omega_1$. By equating $|S_{21}|$ to $|S'_{21}|$ at $\omega = \omega_1$, we can obtain $J'$ value that allows the circuit in Fig. 3 to approximately replicate the response of the circuit in Fig. 2, and it is given by

$$J' = \sqrt{\frac{2(1-\cos\theta)}{\sin\theta}\left(\omega_1(C'-C) - \frac{1}{\omega_1}\left(\frac{1}{L'} - \frac{1}{L}\right)\right)}. \tag{17}$$

Table I shows the parameters of the circuit in Fig. 3 for replicating the responses of the circuit in Fig. 2. $C'$ has been arbitrarily chosen to be 1591.5 pF and the other parameters, $L'$ and $J'$, have been obtained from (13), (16), and (17). Obviously, other sets of the parameters can also be found by having different values for $C'$.

For validating our equations, the responses of the circuit in Fig. 3 and those of the circuit in Fig. 2 having parameters obtained from (13), (16), and (17) have been compared. Fig. 4 confirms that the circuits in Figs. 2 and 3 are equivalent to each other over a frequency range of interest.

For various phase shift values, the equivalent denormalized external coupling value can be extracted using the method described in [19]–[22] and it is shown in Fig. 5. In Fig. 5, external coupling value, $k_{ex}$, has the maximum and minimum value (zero) when the phase shift, $\theta$, is $(2n-1)\pi$ and $2n\pi$, respectively. The operating principle of the coupling structure can also be explained from intuitive perspective. In case of $\theta = 0°$ and $J_1 = -J_2$, the resonator is coupled twice to the same point of the transmission line having opposite signs for the couplings. It is obvious that the net coupling becomes zero since two couplings cancel out. In other words, there is a perfect destructive interaction between the two couplings. When $\theta$ increases from zero, this destructive interaction is not perfect and gives a nonzero coupling. When $\theta = 180°$, the perfect constructive interaction takes place leading to the maximum coupling value. When $\theta = 360°$, the net coupling value becomes zero again, since $\theta = 360°$ is equivalent to $\theta = 0°$.

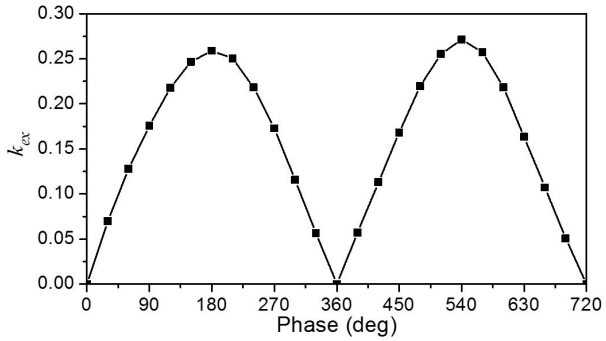


Fig. 5. Equivalent denormalized external coupling value when $J_1$ and $J_2$ have different signs ($J_1 = -J_2 = 1$).

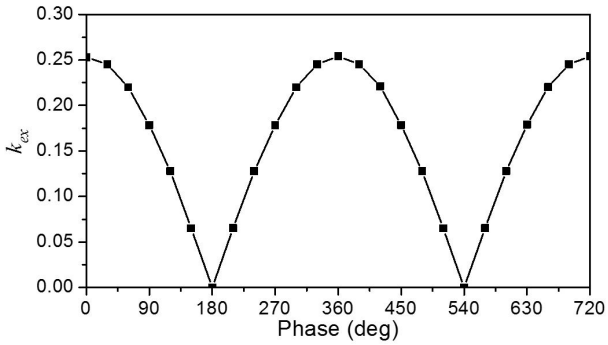


Fig. 6. Equivalent denormalized external coupling value when $J_1$ and $J_2$ have the same sign ($J_1 = J_2 = 1$).

When the two inverter values have the same sign, a different characteristic can be observed. Fig. 6 shows the denormalized external coupling value for the case that $J_1 = J_2 = 1$. It is worth noting that the behavior of the circuit response when $J_1 = J_2$ is 180° off from the one when $J_1 = -J_2$.

In this section, two cases have been considered: $J_1 = -J_2 = 1$ and $J_1 = J_2 = 1$. The two sets have been chosen arbitrarily for demonstrating the presented theory. One can consider more cases with different values and one can observe the behavior of the circuit by plotting the $S_{21}$ response with the aid of (10) and (12). Overall, it can be concluded that the overall external coupling value of a frequency-tunable resonator can be controlled by means of adjusting the phase shift within two reference points where coupling takes place.

## III. VERIFICATION

### A. Resonator Design

In this paper, a single-resonator structure operating from 2.8 to 3.4 GHz based on the coupling diagram shown in Fig. 1(b) is designed to verify that the external coupling can be adjusted by changing the phase delay. A frequency-tunable SIW resonator used in this design is shown in Fig. 7. Since this type of resonator structure has been

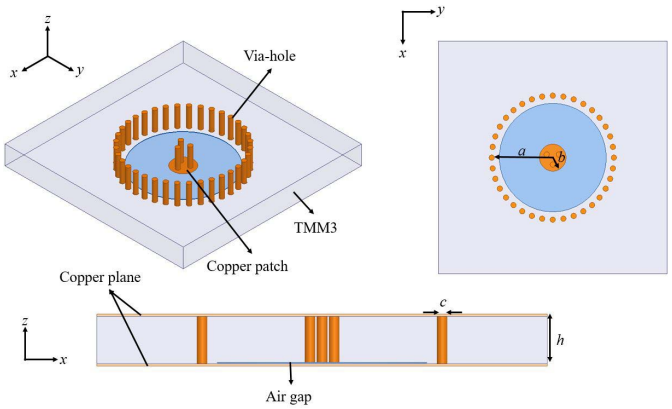


Fig. 7. 3-D view, top view, and cross-sectional side view of the frequency-tunable SIW resonator structure ($a$ = 7.65 mm, $b$ = 1.74 mm, $c$ = 0.7 mm, and $h$ = 3.175 mm). Top and bottom copper planes are not shown in 3-D and top views to expose the inner structure.

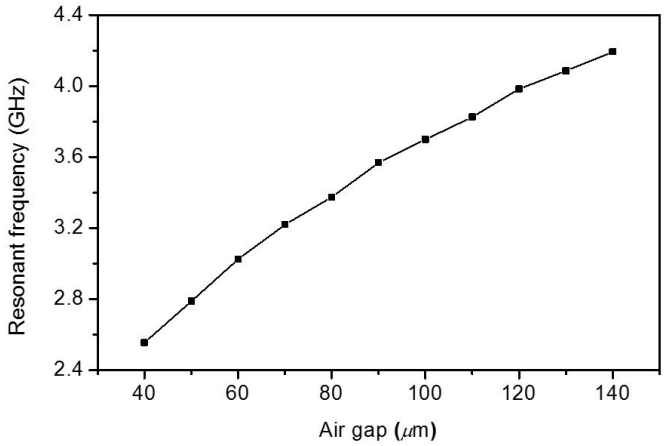


Fig. 8. Resonant frequency as a function of the air-gap thickness.

widely employed in frequency-tunable filter designs [17]–[19], [23]–[25], we give a discussion on our resonator design briefly. The resonator in this design is integrated in a 3.175-mm-thick Rogers TMM3 substrate ($\epsilon = 3.27, \tan\delta = 0.002$). Its side wall is formed by copper-plated via-holes on the boundary, which are connected to both upper and lower copper sheets. A conductive post is loaded at the center of the resonator that is formed by via-holes and a circular copper patch. An air gap is formed between the copper patch and the lower copper sheet, and the existence of this air gap allows the copper sheet to move in the vertical direction, which in turn leads to variation of the resonant frequency. The fundamental mode is used in this paper, and its resonant frequency is shown in Fig. 8 as a function of the air-gap thickness. From Fig. 8, it can be concluded that the deflection of the lower copper sheet by amount of 31 $\mu$m covers the predefined operating range from 2.8 to 3.4 GHz.

### *B. Phase Shifter*

To obtain a certain amount of phase shift between the two ports depicted in Fig. 2, we use the continuously tunable phase shifter presented in [26]. The circuit schematic of the phase shifter is shown in Fig. 9. It has two quarter-wavelength

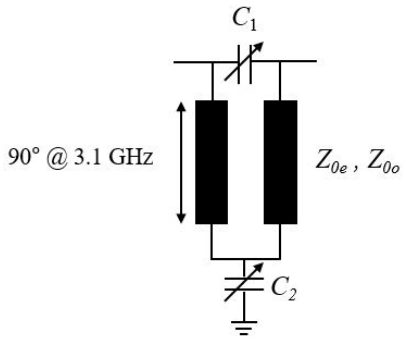


Fig. 9. Analog phase shifter using two varactors.

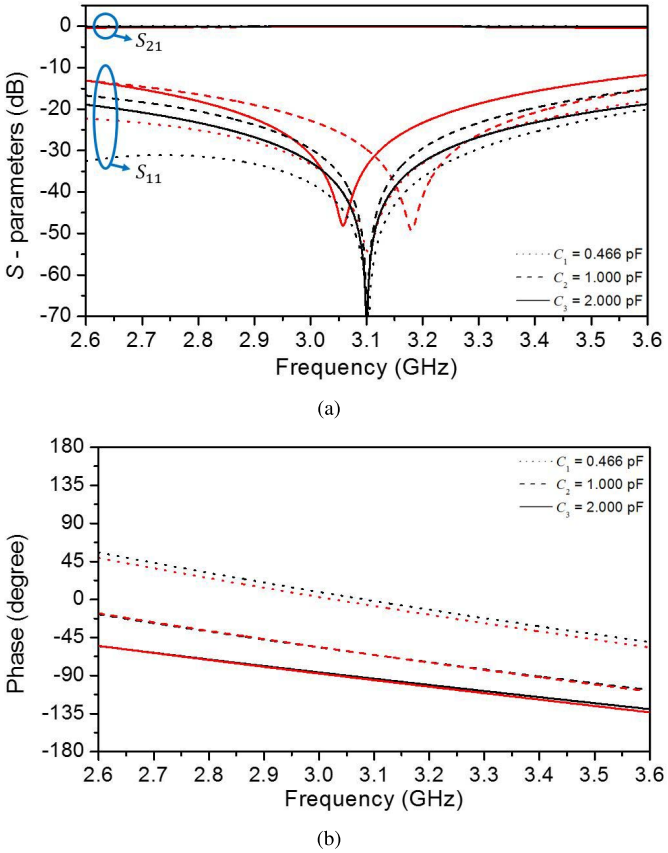


Fig. 10. Frequency responses of the phase shifters shown in Figs. 9 and 11. (a) Magnitude. (b) Phase.

transmission lines and two varactors. Considering the target frequency tuning range, the length of each line has been determined such that it is a quarter wavelength at 3.1 GHz. It is reported that an excellent impedance matching can be obtained when the capacitance of varactor $C_2$ doubles that of $C_1$ and $Z_{0e}$ = 58.4 Ω and $Z_{0o}$ = 40.3 Ω [26]. The black lines in Fig. 10(a) and (b) show the magnitude and wrapped phase responses of the ideal circuit schematic shown in Fig. 9, respectively. It can be concluded that the phase can be controlled by varying the capacitance values while maintaining a good impedance matching performance. In this paper, we implement the phase shifter on a 0.508-mm-thick Rogers 4350B substrate ($\epsilon = 3.66, \tan\delta = 0.004$), and its structure is shown in Fig. 11. $C_1$ and $C_2$ are implemented by

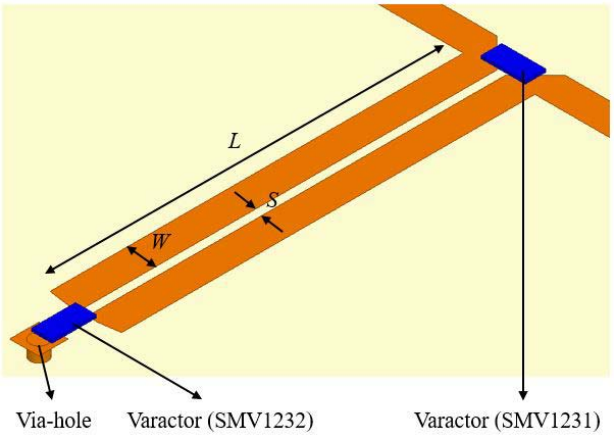


Fig. 11. Microstrip line analog phase shifter ($L$ = 14.1 mm, $W$ = 1.1 mm, and $S$ = 0.3 mm).

two varactors, SMV1231-079LF and SMV1232-079LF, from Skyworks whose tuning ranges are from 0.466 to 2.35 pF, and from 0.72 to 4.15 pF, respectively.

The practical circuit shown in Fig. 11 contains parasitics that are not included in the ideal circuit model shown in Fig. 9. Hence, the impedance matching condition for the practical circuit is different from the one for the ideal circuit model, and it was found to be $C_2 = 1.78C_1$. The red lines in Fig. 10 show the frequency responses of the circuit shown in Fig. 11 for various sets of the capacitor values. Again, the phase shift can be controlled having a good return loss over the frequency range of interest.

### C. Filter

A first-order bandstop filter using the resonator structure and phase shifter described in Sections III-A and III-B, respectively, has been designed for verifying the presented coupling structure shown in Fig. 2. Two substrates containing the phase shifter and resonator are stacked as shown in Fig. 12. The resonator is coupled to the line through two coupling slots that correspond to two $J$ inverters in Fig. 2. As discussed above, the overall external coupling value can be adjusted by controlling the two varactors, and Fig. 13 shows the external coupling value of the structure shown in Fig. 12 for various coupling slot angles when the notch is centered at 3.1 GHz. In this paper, the slot angle has been chosen to be 90° so that the external coupling has a wide tuning range including zero. The capacitive patches are constructed in the line above the coupling slots for compensating the impedance variation caused by creating the slots [27]. Fig. 14 shows the full-wave simulation responses of the first-order bandstop filter. It depicts that a different set of varactor capacitances leads to a different bandwidth, which in turn indicates that the overall external value varies with the phase shift from one slot to the other.

## IV. Fabrication and Measurement

For verifying the presented theory, the first-order bandstop filter shown in Fig. 12 has been fabricated. The fabricated filter is shown in Fig. 15. The upper layer has been fabricated by drilling and plating via-holes followed by etching the

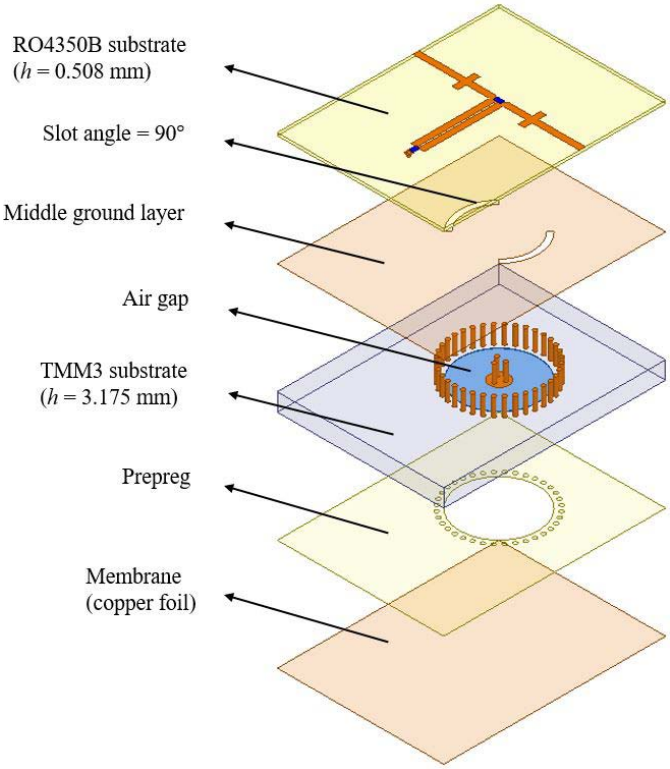


Fig. 12. Layer-by-layer view of the first-order bandstop filter structure.

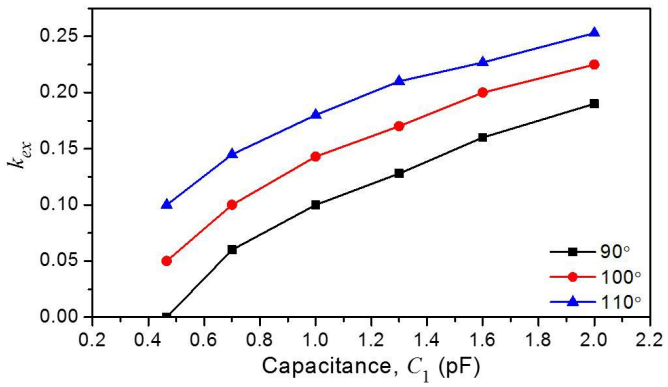


Fig. 13. External coupling value of the first-order filter for various coupling slot angles.

substrate for creating the transmission line. It contains two varactors for adjusting the phase shifter. For dc biasing, dc block capacitors (2400 pF) and 10-kΩ resistors are also placed in this upper layer. Since fabricating the resonator structure has been discussed in numerous papers [17], [19], [28], [29], discussing it is not repeated in this paper. A piezoelectric linear actuator is attached to the bottom side of the resonator structure for the purpose of adjusting the air-gap thickness between the copper post and the copper plane on the bottom side. Hence, the resonant frequency of the resonator can be controlled.

For providing the measured results of the phase shifter, we have also fabricated a stand-alone phase shifter, and its measured responses are shown in Fig. 16. It has an insertion

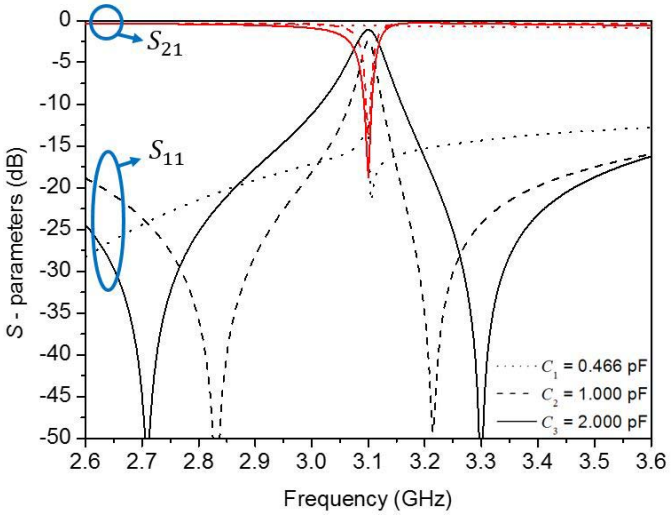


Fig. 14. Simulated frequency responses of the first-order bandstop filter.

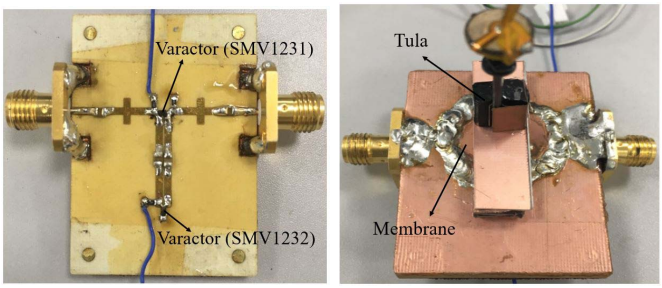


(a) (b)

Fig. 15. (a) Top view and (b) bottom view of the fabricated first-order bandstop filter.

loss smaller than 1.5 dB and a return loss better than 16.2 dB. De-embedding process has been conducted to extract the phase shift from the reference plane of one slot to that of the other. This process excludes the phase delay produced by the coaxial connectors and the lines up to the slots. Since the phase responses shown in Fig. 16(b) are the wrapped ones, they are plotted within the range from $-180°$ to $+180°$. Unwrapping these, we obtained 375°, 431°, and 465° at 3.1 GHz when $C_1$ is 0.466, 1.000, and 2.000 pF, respectively.

Fig. 17(a) compares the measured results and simulated results of the first-order filter when centered at 3.1 GHz. It can be reconfigured to have a different bandwidth and Fig. 17(b) shows that the 3 dB bandwidth ranges from 0 (effectively all-pass responses) to 62.2 MHz. This implies that the overall external coupling value of the resonator can be adjusted by controlling the phase delay from one coupling slot to the other. By virtue of the frequency-tunable feature of the resonator, the stopband can be relocated as shown in Fig. 18(a) and (b).

## V. Application

A second-order frequency- and bandwidth-tunable bandstop filter has been designed for verifying the presented theory and structure for the tunable external coupling structure between a transmission line and a resonator. Fig. 19(a) shows the

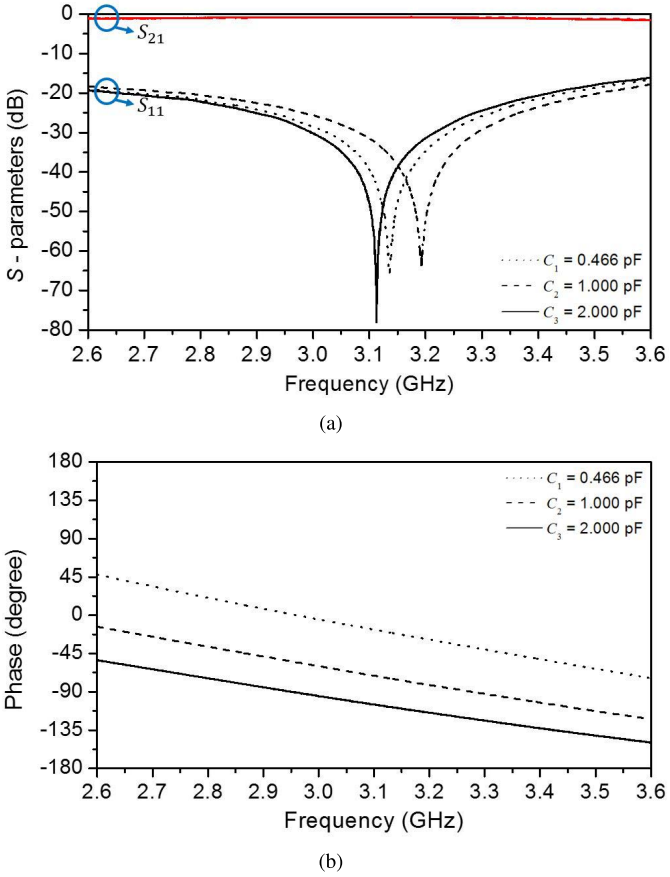


Fig. 16. Measured responses of the phase shifter. (a) Magnitude. (b) Phase.

conventional circuit model for a second-order tunable bandstop filter. A uniform transmission line runs from the input port to the output port, and it is coupled to two frequency-tunable resonators via tunable external coupling structures. The two resonators are separated by an odd multiple of a quarter wavelength along the line. The normalized coupling matrix corresponding to the circuit model shown in Fig. 19(a) is given by

$$\mathbf{M} = \begin{bmatrix} 0 & M_{S1} & 0 & M_{SL} \\ M_{S1} & 0 & 0 & 0 \\ 0 & 0 & 0 & M_{2L} \\ M_{SL} & 0 & M_{2L} & 0 \end{bmatrix} \tag{18}$$

where $S$ and $L$ represent the source and load, respectively, and the numbers represent the resonators. $M_{S1}$ and $M_{2L}$ are the normalized external coupling values between the line and each resonator, and $M_{SL}$ is the normalized coupling between the input and output ports. The matrix element values can be obtained by using well-known filter synthesis techniques [30], [31] and they are $M_{S1} = M_{2L} = 1.189$ and $M_{SL} = 1.000$ for the Butterworth response. The denormalized external coupling values are then [19]

$$k_{S1} = k_{2L} = M_{S1}\sqrt{\frac{\Delta}{2}} = M_{2L}\sqrt{\frac{\Delta}{2}} \tag{19}$$

where $\Delta$ is the design fractional bandwidth. For designing a bandwidth-tunable bandstop filter, it is obvious that the external coupling structures are required to be adjustable.

TABLE II
COMPARISON WITH PUBLISHED WORKS

| Ref. | Resonator type | Order | Frequency tuning range (GHz) | 3 dB bandwidth tuning range (MHz) | Individual external coupling control | Zero coupling for all-pass response |
|---|---|---|---|---|---|---|
| [14] | Microstrip | 2 | 0.9 - 1.2 | 25 - 100 @ 0.9 GHz | Possible | Impossible |
| [15] | Coaxial stepped-impedance | 2 | 2.15 - 2.75 | 250 - 480 @ 2.45 GHz | Possible | Impossible |
| [15] | Coaxial stepped-impedance | 3 | 1.9 - 2.3 | 160 - 250 @ 2.15 GHz | Possible | Impossible |
| [16] | SIW | 2 | 0.77 - 1.25 | 20 - 85 @ 0.77 GHz | Possible | Impossible |
| [18] | SIW | 4 | 2.4 - 3.6 | 100 - 165 @ 3.23 GHz | Impossible | Impossible |
| This work | SIW | 1 | 2.8 - 3.4 | 0 - 62.2 @ 3.1 GHz | Possible | Possible |
| This work | SIW | 2 | 2.8 - 3.4 | 0 - 96 @ 3.1 GHz | Possible | Possible |

∗ Some numbers are obtained by reading plots.

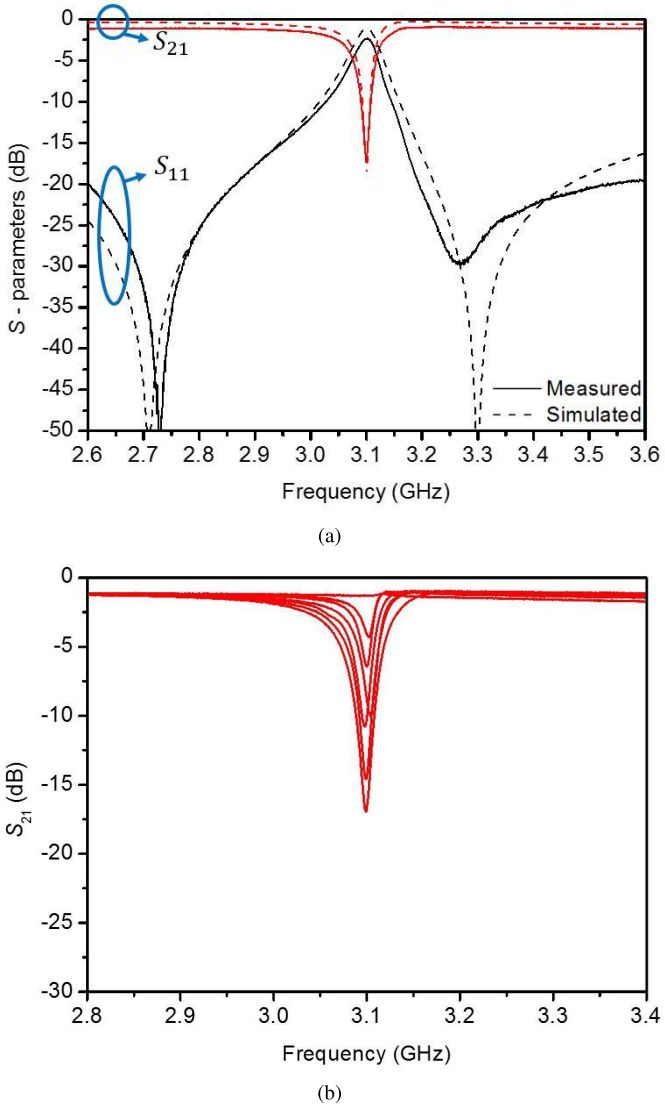


Fig. 17. (a) Measured and simulated responses of the first-order bandstop filter. (b) Measurement with bandwidth tuning at 3.1 GHz.

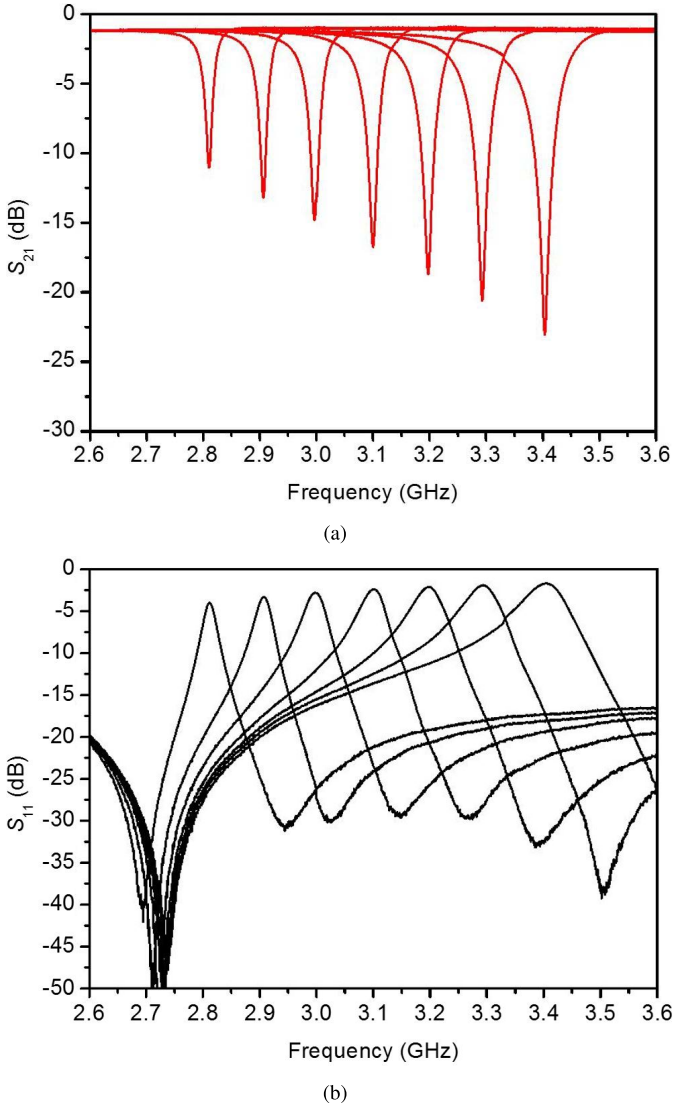


Fig. 18. Measured frequency responses of the first-order bandstop filter. (a) Transmission. (b) Reflection.

Hence, we adopt tunable external coupling structure presented in Section II, and Fig. 19(b) shows the equivalent circuit model that contains the presented tunable external coupling structures. The resonator and phase shifter structures described

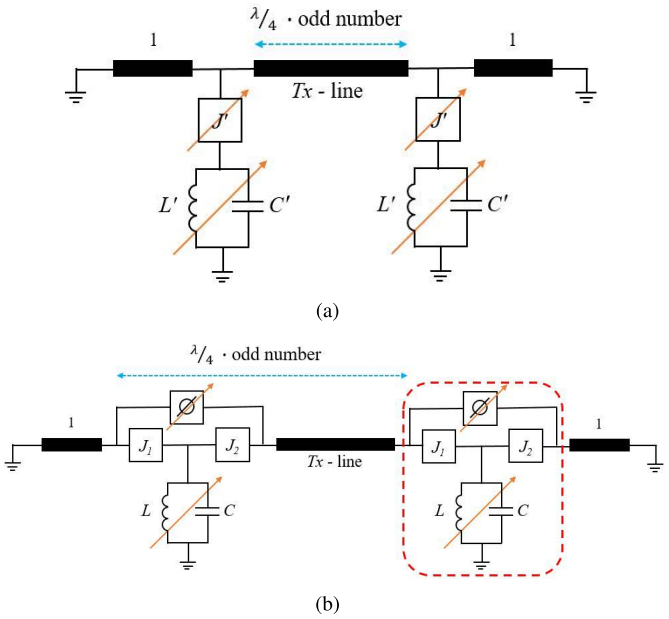


Fig. 19. (a) Circuit model of the second-order tunable bandstop filter. (b) Proposed circuit model.

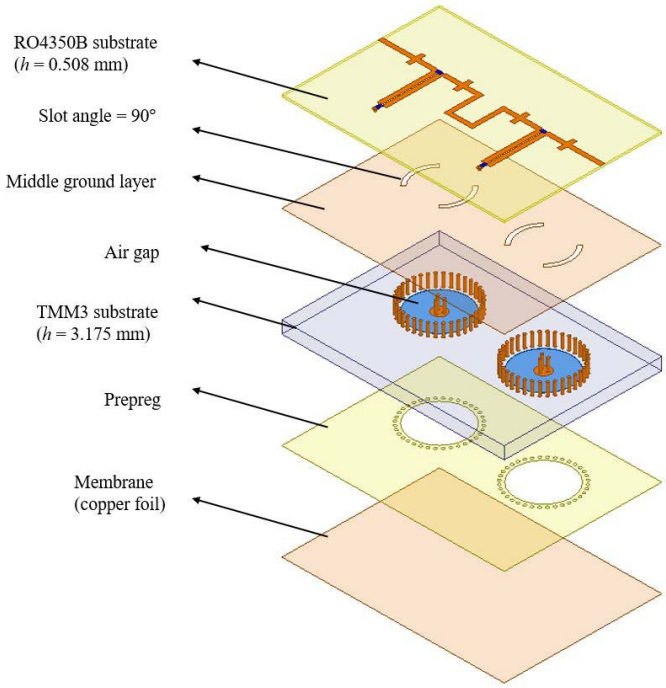


Fig. 20. Layer-by-layer view of the second-order bandstop filter structure.

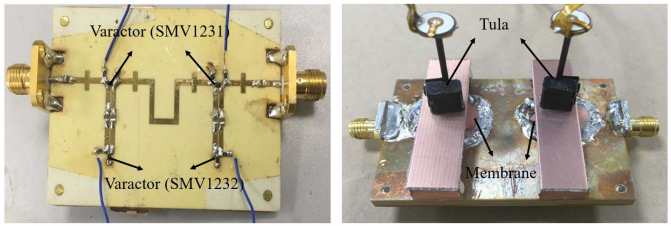


Fig. 21. (a) Top view and (b) bottom view of the fabricated second-order bandstop filter.

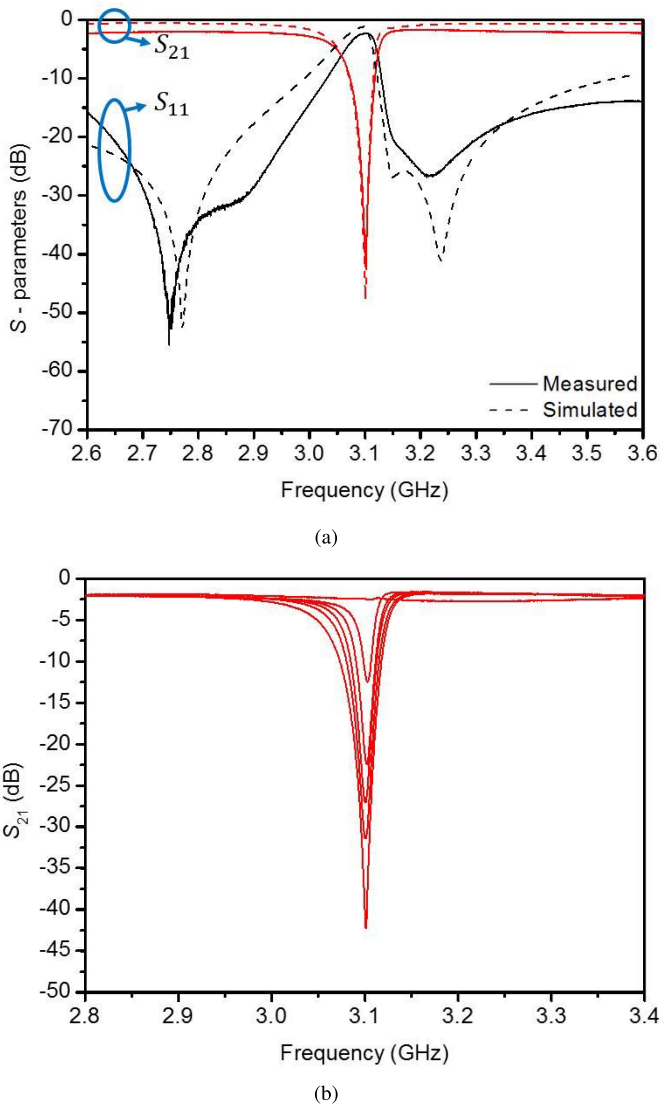


Fig. 22. (a) Measured and simulated responses of the second-order bandstop filter. (b) Measurement with bandwidth tuning at 3.1 GHz.

in Section III are used in designing a second-order bandstop filter that corresponds to the circuit model shown in Fig. 19(b). Fig. 20 shows the layer-by-layer view of the second-order bandstop filter. There exists a meandering microstrip line on the top layer and this corresponds to the transmission line in the middle of the circuit model shown in Fig. 19(b). The length of this microstrip line is determined to be 26.8 mm so that the line length from the reference plane of the first resonator to the one of the second resonator is an odd multiple of a quarter wavelength. The other dimensions are identical to the ones shown in Figs. 7 and 11. Fig. 21 shows the fabricated second-order bandstop filter. Fig. 22(a) shows the measured and simulated responses of the filter centered at 3.1 GHz when the external coupling structures have the maximum coupling value leading to a maximum bandwidth of 96 MHz. The

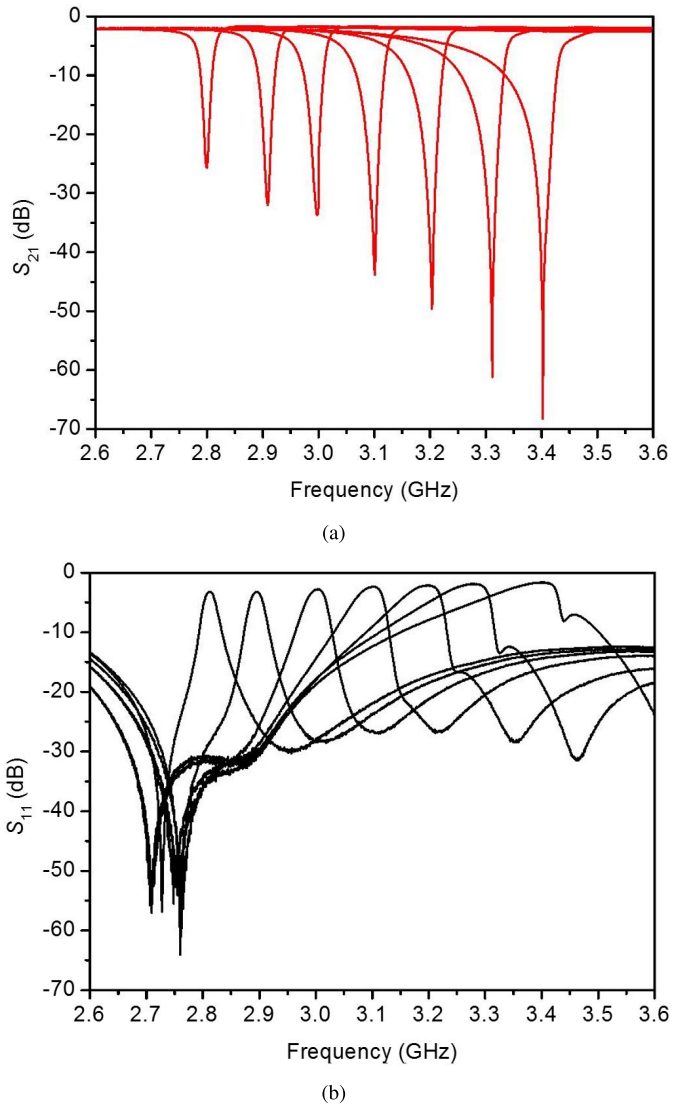


Fig. 23. Measured frequency responses of the second-order bandstop filter. (a) Transmission. (b) Reflection.

bandwidth can be controlled by adjusting the phase shifters and the measurement of the bandwidth tuning at 3.1 GHz is shown in Fig. 22(b). It is worth noting that the bandwidth can be reduced down to 0 MHz resulting in the all-pass response. Since the bandstop filter has the frequency-tunable resonators, the stopband can be tuned from 2.8 to 3.4 GHz as shown in Fig. 23. The asymmetric responses in Fig. 23 can be attributed to the frequency-dependent behavior of the transmission line [27], [32].

This paper has been compared with the published works, and the comparison is summarized in Table II. It is worth emphasizing that obtaining the zero coupling for realizing the all-pass response is feasible in the filter structures.

## VI. Conclusion

In this paper, we have first presented a new tunable external coupling structure between a transmission line and an SIW resonator. The resonator is coupled to the line via two coupling slots and the phase shift between the two slots determines the overall effective coupling between the line and the resonator. The presented coupling structure has been rigorously analyzed by means of using an equivalent circuit model. The measurement has verified the presented tunable external coupling structure, and it has been applied to the design of a frequency- and bandwidth-tunable second-order bandstop filter. The fabricated filter has a bandwidth tuning range from 3.1% when centered at 3.1 GHz and the center frequency tuning range from 2.8 to 3.4 GHz.

## References

[1] J. Lee and K. Sarabandi, "An analytic design method for microstrip tunable filters," *IEEE Trans. Microw. Theory Techn.*, vol. 56, no. 7, pp. 1699–1706, Jul. 2008.

[2] J. Lee, E. J. Naglich, H. H. Sigmarsson, D. Peroulis, and W. J. Chappell, "Tunable inter-resonator coupling structure with positive and negative values and its application to the field-programmable filter array (FPFA)," *IEEE Trans. Microw. Theory Techn.*, vol. 59, no. 12, pp. 3389–3400, Dec. 2011.

[3] Y.-H. Cho and G. M. Rebeiz, "0.73–1.03-GHz tunable bandpass filter with a reconfigurable 2/3/4-pole response," *IEEE Trans. Microw. Theory Techn.*, vol. 62, no. 2, pp. 290–296, Feb. 2014.

[4] Y.-C. Chiou and G. M. Rebeiz, "Tunable 1.55–2.1 GHz 4-pole elliptic bandpass filter with bandwidth control and >50 dB rejection for wireless systems," *IEEE Trans. Microw. Theory Techn.*, vol. 61, no. 1, pp. 117–124, Jan. 2013.

[5] J.-R. Mao, W.-W. Choi, K.-W. Tam, W. Q. Che, and Q. Xue, "Tunable bandpass filter design based on external quality factor tuning and multiple mode resonators for wideband applications," *IEEE Trans. Microw. Theory Techn.*, vol. 61, no. 7, pp. 2574–2584, Jul. 2013.

[6] H. Joshi, H. H. Sigmarsson, S. Moon, D. Peroulis, and W. J. Chappell, "High-fully reconfigurable tunable bandpass filters," *IEEE Trans. Microw. Theory Techn.*, vol. 57, no. 12, pp. 3525–3533, Dec. 2009.

[7] A. Anand and X. Liu, "Substrate-integrated coaxial-cavity filter with tunable center frequency and reconfigurable bandwidth," in *Proc. IEEE 15th Wireless Microw. Technol. Conf.*, Jun. 2014, pp. 1–4.

[8] B. You, S. Lu, L. Chen, and Q. Gu, "A half-mode substrate-integrated filter with tunable center frequency and reconfigurable bandwidth," *IEEE Microw. Wireless Compon. Lett.*, vol. 26, no. 3, pp. 189–191, Feb. 2016.

[9] Y.-C. Ou and G. M. Rebeiz, "Lumped-element fully tunable bandstop filters for cognitive radio applications," *IEEE Trans. Microw. Theory Techn.*, vol. 59, no. 10, pp. 2461–2468, Oct. 2011.

[10] W. Yan and R. Mansour, "Compact tunable bandstop filter integrated with large deflected actuators," in *IEEE MTT-S Int. Microw. Symp. Dig.*, Jun. 2007, pp. 1611–1614.

[11] C. Rauscher, "Varactor-tuned active notch filter with low passband noise and signal distortion," *IEEE Trans. Microw. Theory Techn.*, vol. 49, no. 8, pp. 1431–1437, Aug. 2001.

[12] M. F. Karim, A. Q. Liu, A. B. Yu, and A. Alphones, "MEMS-based tunable bandstop filter using electromagnetic bandgap (EBG) structures," in *Proc. Asia–Pacific Conf. Microw. Conf. (APMC)*, vol. 3. Dec. 2005, p. 4.

[13] X. Y. Zhang, C. H. Chan, Q. Xue, and B. J. Hu, "RF tunable bandstop filters with constant bandwidth based on a doublet configuration," *IEEE Trans. Ind. Electron.*, vol. 59, no. 2, pp. 1257–1265, Feb. 2012.

[14] D. Psychogiou, R. Gómez-García, and D. Peroulis, "A class of fully-reconfigurable planar multi-band bandstop filters," in *IEEE MTT-S Int. Microw. Symp. Dig.*, May 2016, pp. 1–4.

[15] T. Yang and G. M. Rebeiz, "Bandpass-to-bandstop reconfigurable tunable filters with frequency and bandwidth controls," *IEEE Trans. Microw. Theory Techn.*, vol. 65, no. 7, pp. 2288–2297, Jul. 2017.

[16] A. Anand and X. Liu, "Capacitively tuned electrical coupling for reconfigurable coaxial cavity bandstop filters," in *IEEE MTT-S Int. Microw. Symp. Dig.*, May 2015, pp. 1–3.

[17] J. Lee, E. J. Naglich, and W. J. Chappell, "Frequency response control in frequency-tunable bandstop filters," *IEEE Microw. Wireless Compon. Lett.*, vol. 20, no. 12, pp. 669–671, Dec. 2010.

[18] E. J. Naglich, J. Lee, D. Peroulis, and W. J. Chappell, "High-$Q$ tunable bandstop filters with adaptable bandwidth and pole allocation," in *IEEE MTT-S Int. Microw. Symp. Dig.*, Jun. 2011, pp. 1–4.

[19] J. Lee, E. J. Naglich, H. H. Sigmarsson, D. Peroulis, and W. J. Chappell, "New bandstop filter circuit topology and its application to design of a bandstop-to-bandpass switchable filter," *IEEE Trans. Microw. Theory Techn.*, vol. 61, no. 3, pp. 1114–1123, Mar. 2013.
[20] D. Kajfez and E. J. Hwan, "Q-factor measurement with network analyzer," *IEEE Trans. Microw. Theory Techn.*, vol. MTT-32, no. 7, pp. 666–670, Jul. 1984.
[21] D. Kajfez and P. Guillon, *Dielectric Resonators*. Norwood, MA, USA: Artech House, 1986.
[22] A. Khanna and Y. Garault, "Determination of loaded, unloaded, and external quality factors of a dielectric resonator coupled to a microstrip line," *IEEE Trans. Microw. Theory Techn.*, vol. MTT-31, no. 3, pp. 261–264, Mar. 1983.
[23] V. Sekar, M. Armendariz, and K. Entesari, "A 1.2–1.6-GHz substrate-integrated-waveguide RF MEMS tunable filter," *IEEE Trans. Microw. Theory Techn.*, vol. 59, no. 4, pp. 866–876, Apr. 2011.
[24] M. Armendariz, V. Sekar, and K. Entesari, "Tunable SIW bandpass filters with pin diodes," in *Proc. Eur. Microw. Conf.*, Sep. 2010, pp. 830–833.
[25] S. Saeedi, J. Lee, and H. H. Sigmarsson, "Novel coupling matrix synthesis for single-layer substrate-integrated evanescent-mode cavity tunable bandstop filter design," *IEEE Trans. Microw. Theory Techn.*, vol. 63, no. 12, pp. 3929–3938, Dec. 2015.
[26] K. Khoder, A. Pérennec, and M. Roy, "A 180° tunable analog phase shifter based on a single all-pass unit cell," *Microw. Opt. Technol. Lett.*, vol. 55, no. 12, pp. 2915–2918, Sep. 2013.
[27] E. J. Naglich, J. Lee, D. Peroulis, and W. J. Chappell, "Extended pass-band bandstop filter cascade with continuous 0.85–6.6-GHz coverage," *IEEE Trans. Microw. Theory Techn.*, vol. 60, no. 1, pp. 21–30, Jan. 2012.
[28] E. J. Naglich, J. Lee, D. Peroulis, and W. J. Chappell, "Switchless tunable bandstop-to-all-pass reconfigurable filter," *IEEE Trans. Microw. Theory Techn.*, vol. 60, no. 5, pp. 1258–1265, May 2012.
[29] B. Lee, S. Nam, B. Koh, C. Kwak, and J. Lee, "K-band frequency tunable substrate-integrated-waveguide resonator filter with enhanced stopband attenuation," *IEEE Trans. Microw. Theory Techn.*, vol. 63, no. 11, pp. 3632–3640, Nov. 2015.
[30] R. J. Cameron, C. M. Kudsia, and R. R. Mansour, *Microwave Filters for Communication Systems*. New York, NY, USA: Wiley, 2007.
[31] J.-S. Hong and M. L. Lancaster, *Microstrip Filters for RF/Microwave Applications*. New York, NY, USA: Wiley, 2001.
[32] I. C. Hunter and J. D. Rhodes, "Electronically tunable microwave bandstop filters," *IEEE Trans. Microw. Theory Techn.*, vol. MTT-30, no. 9, pp. 1361–1367, Sep. 1982.

**Seong-Wook Jeong** received the B.E. degree in computer and communication engineering from Korea University, Seoul, South Korea, in 2016, where he is currently pursuing the Ph.D. degree in radio communications engineering.

His current research interests include tunable microwave components and RF communication systems.

**Juseop Lee** (A'02–M'03–SM'16) received the B.E. and M.E. degrees in radio science and engineering from Korea University, Seoul, South Korea, in 1997 and 1999, respectively, and the Ph.D. degree in electrical engineering from the University of Michigan, Ann Arbor, MI, USA, in 2009.

He joined the Electronics and Telecommunications Research Institute, Daejeon, South Korea, in 2001, where he was involved in the design of passive microwave equipment for Ku- and Ka-band communications satellites. In 2005, he joined the University of Michigan, where he was a Research Assistant and a Graduate Student Instructor with the Radiation Laboratory, and was involved in research activities focused on millimeter-wave radars and synthesis techniques for multiple-passband microwave filters. In 2009, he joined Purdue University, West Lafayette, IN, USA, where he was a Post-Doctoral Research Associate, which included involvement with the design of adaptable RF systems. In 2012, he joined Korea University, where he is currently an Associate Professor. His current research interests include RF and microwave components, satellite transponders, wireless power transfer, and electromagnetic theories.

Prof. Lee was the recipient of the Graduate Fellowship from the Korea Science and Engineering Foundation, Daejeon, and the Rackham Pre-Doctoral Fellowship from the Rackham Graduate School, University of Michigan. He was a recipient of the IEEE Microwave Theory and Techniques Society Graduate Fellowship. He is currently an Associate Editor for the IEEE TRANSACTIONS ON MICROWAVE THEORY AND TECHNIQUES.